The Astrophysical Journal Letters, 987:L34 (7pp), 2025 July 10 https://doi.org/10.3847/2041-8213/ade5a8

Highly Polarized Type III Storm Observed with Parker Solar Probe

Marc Pulupa[1], Stuart D. Bale[1,2], Immanuel Christopher Jebaraj[3], Orlando Romeo[1], and Säm Krucker[1,4]
[1] Space Sciences Laboratory, University of California, Berkeley, CA 94720-7450, USA; pulupa@berkeley.edu
[2] Physics Department, University of California, Berkeley, CA 94720-7300, USA
[3] Space Research Laboratory, University of Turku, Turku, Finland
[4] University of Applied Sciences and Arts Northwestern Switzerland, Bahnhofstrasse 6, 5210 Windisch, Switzerland

Received 2024 December 6; revised 2025 June 10; accepted 2025 June 18; published 2025 July 7

Abstract

The Parker Solar Probe (PSP) spacecraft observed a large coronal mass ejection (CME) on 2022 September 5, shortly before closest approach during the 13th PSP solar encounter. For several days following the CME, PSP detected a storm of Type III radio bursts. Stokes parameter analysis of the radio emission indicates that the Type III storm was highly circularly polarized (with fractional polarization up to ∼0.4). Left-hand circularly polarized (LHC) emission dominated at the start of the storm, transitioning to right-hand circularly polarized (RHC) emission at the crossing of the heliospheric current sheet on September 6. We analyze the properties of this Type III storm. The drift rate of the Type IIIs indicates a constant beam speed of ∼0.1c, typical for Type III-producing electron beams. The sense of polarization is consistent with fundamental emission generated primarily in the O-mode. The stable and well organized post-CME magnetic field neatly separates the LHC- and RHC-dominated intervals of the storm, with minimal overlap between the senses of polarization. The proximity of PSP to the source region, both in radial distance and in heliographic longitude, makes this event an ideal case study to connect in situ plasma measurements with remote observations of radio emission.

Unified Astronomy Thesaurus concepts: Solar radio emission (1522); Radio bursts (1339); Space vehicle instruments (1548)

1. Introduction

Type III solar radio emission is generated by beams of electrons accelerated near the Sun (G. A. Dulk 2000; H. A. S. Reid & H. Ratcliffe 2014). Type III emission can occur as discrete individual bursts or as a Type III storm, a quasi-continuous series of small bursts. Type III storms typically last for several days and in some cases longer than a full solar rotation (J. Fainberg & R. G. Stone 1970a, 1970b, 1971). Interplanetary (IP) Type III storms are typically a low-frequency extension of "metric" Type III storms, which occur at higher frequencies, with a solar active region as the common source for both the IP and metric storms. The persistence of storm emission is indicative of a stable active region configuration, which is favorable for accelerating electrons into IP space (J. L. Bougeret et al. 1984a, 1984b; R. P. Lin 1985; M. J. Reiner et al. 2001; N. Gopalswamy 2004; J. P. Eastwood et al. 2010). Radio observations and imaging provide evidence that Type III storms are generated near the boundary of active regions (A. Morioka et al. 2007; L. Harra et al. 2021).

Reconfiguration of the magnetic field—for example, by a coronal mass ejection (CME)—can disrupt a Type III storm, causing cessation of the storm activity (M. J. Reiner et al. 2001; N. Gopalswamy 2004). B. Ma et al. (2025) found that Type III storms occurring post-CME have a gradual change in intensity akin to Type IV radio emission and that they are highly structured. The latter is similar to regular Type III bursts observed by the Parker Solar Probe (PSP; I. C. Jebaraj et al. 2023; C. P. Sishtla et al. 2023). This indicates that the global morphology of the storms is affected by transient events, while individually they are strongly characterized by Type III properties.

In this Letter, we present a Type III storm observed by the PSP spacecraft during the 13th PSP solar encounter, with a focus on the circular polarization of the storm radio emission and the dependence of that polarization on the magnetic field in the emission region.

2. Data

The PSP spacecraft (N. J. Fox et al. 2016) launched in 2018 into an elliptical orbit around the Sun, with a perihelion significantly closer to the solar surface than any previous spacecraft. PSP completed its thirteenth solar encounter (E13) during 2022 September, with a perihelion distance of 13.3 $R_\odot$.

We use magnetic field and radio data from the PSP/FIELDS instrument suite (S. D. Bale et al. 2016). Radio measurements are made with the FIELDS Radio Frequency Spectrometer (RFS; M. Pulupa et al. 2017). During E13, one channel of the two-channel RFS receiver made measurements from the $V1 - V2$ dipole and the other channel from the $V3 - V4$ dipole. A diagram of this "cross-dipole" configuration can be found in B. Page et al. (2022).

The RFS produces data in two frequency ranges. The low-frequency receiver (LFR) range covers a bandwidth of 10 kHz–1.7 MHz, and high-frequency receiver (HFR) data cover 1.3–19.2 MHz. During E13, both LFR and HFR spectra were produced at a cadence of approximately 3.5 s per spectrum. During sustained periods of continuous high-amplitude signals, the cadence of spectra can slow to 7 s per spectrum. This study focuses on radio emission in the HFR frequency range, where the circular polarization signal is most prominent. LFR data are used to determine the in situ electron density (M. Moncuquet et al. 2020).

All RFS data products in this Letter use Level 3 RFS data. In Level 3 data, corrections are applied to account for higher noise background during low-gain intervals, instrument noise from the preamplifier and analog components in the receiver is removed, and the antenna effective length determined by B. Page et al. (2022) is used to convert spectral quantities to physical units of $\mathrm{W\,m^{-2}\,Hz^{-1}}$.

2.1. Circular Polarization

Using the auto- and cross-spectral data together allows us to construct Stokes parameters, which describe the intensity and polarization of the observed radio emission. We focus on the Stokes V parameter, a signed quantity that describes the intensity of circularly polarized emission (T. Robishaw & C. Heiles 2021). Stokes V is often presented normalized to the Stokes intensity I, where fully circularly polarized emission would have a V/I value of -1 or 1.

Since its launch, PSP has observed circularly polarized emission in individual Type III bursts (M. Pulupa et al. 2020; N. Dresing et al. 2023; I. C. Jebaraj et al. 2023), Type III storms (M. Pulupa et al. 2020), and Type II radio bursts driven by CMEs (T. Nieves-Chinchilla et al. 2022). Reported observations of polarized IP solar radio emission from other spacecraft, such as Wind (J. L. Bougeret et al. 1995), STEREO (J. L. Bougeret et al. 2008), and Cassini (D. A. Gurnett et al. 2004), are rare. This is likely due to a combination of factors: first, not all radio bursts show significant polarization (N. Dresing et al. 2023). Additionally, the polarized component of emission seen on PSP, for both individual Type III bursts and during Type III storms, is largest at frequencies above several MHz. Wind and STEREO have typically made polarization measurements at lower frequencies. The STEREO spacecraft measures the direction and circular polarization of radio emission up to 2 MHz (B. Cecconi et al. 2008; V. Krupar et al. 2014). Previous Wind polarization measurements (e.g., M. J. Reiner et al. 2007) have been made using the RAD1 receiver, with a maximum frequency of 1.04 MHz.

We note that Stokes V values used in this work result from an updated version of the simplified calculation described in M. Pulupa et al. (2020). The value of V is corrected for the effects of antenna nonorthogonality and nonequal antenna effective length using Mueller matrices, which are 4×4 matrices representing transfer functions between the measured and true Stokes parameters. We define our Mueller matrix corrections using the short dipole approximation, as described in A. Lecacheux (2011). In the Level 3 RFS HFR and LFR data files, the corrected circular polarization is contained in the `STOKES_V` variables. The corrections resulting from the Level 3 noise subtraction and Mueller matrix are typically small: for the spectra analyzed in this Letter, the difference between the Level 3 V and the simpler calculation used in M. Pulupa et al. (2020) is always smaller than 0.01.

We use the convention where Stokes $V > 0$ corresponds to right-hand circularly polarized emission (RHC), while $V < 0$ corresponds to left-hand circular emission (LHC). We note that the works mentioned in the previous paragraph used the opposite convention. This change was implemented during the development of the Level 3 RFS data, in order to be consistent with the IAU definition of the Stokes parameters (J. P. Hamaker & J. D. Bregman 1996; T. Robishaw & C. Heiles 2021). We emphasize that the physical interpretation of the wave handedness has not changed, merely the sign convention for V.

3. Observations

3.1. Context: E13 CME

Shortly before the E13 perihelion in early 2022 September, PSP observed a complex interplanetary coronal mass ejection (ICME). Remote sensing and in situ observations of the CME are described in O. M. Romeo et al. (2023), hereafter referred to as R23. We present here a highly compressed description of the CME timeline described in detail in R23 to provide context for our focused study of the Type III storm.

Remote sensing observations of the CME eruption commence at 09-05/16:10 (t_0 in R23), and the ICME shock arrives in situ at 09-05/17:27 (t_1 in R23). After the shock passage, PSP enters the ICME sheath, followed by a period of closed field lines. After exiting the sheath, the field becomes more stable, with a predominantly outward field from 09-06/03:26 to 09-06/17:28 (t_{5b} and t_{7a} in R23).

The spacecraft then crosses a current sheet (CS) into a region of steady inward field, starting at 09-06/17:40 (t_{7b} in R23). Plasma conditions change abruptly at the CS crossing, with density dropping from >1000 to $\sim 100\,\mathrm{cm^{-3}}$ and velocity decreasing from ~ 350 to $\sim 200\,\mathrm{km\,s^{-1}}$.

The passage of the CME reconfigures the magnetic field, leaving the steady, radial field observed during the interval of the Type III storm. The field inversion, which occurs during the brief interval between t_{7a} and t_{7b}, corresponds to the Carrington longitude (300°) of the active region responsible for the CME (AR 13102, previously named AR 13088).

3.2. Circularly Polarized Radio Burst Storm

Figure 1 shows PSP radio and magnetic field data before, during, and after the September 5 CME. Figure 1(a) shows a spectrogram of intensity, while Figure 1(b) shows the circular polarization. The intensity and polarization spectrograms include data from both the RFS HFR and LFR receivers. On the circular polarization spectrogram, red indicates LHC emission, while blue indicates RHC. Circular polarization is not plotted when the intensity is negligible, for example, at high frequencies (>2 MHz) during the interval before the CME.

Figure 1(c) shows the in situ magnetic field in RTN coordinates, illustrating the disturbed field generated by the CME and the sharp transition in radial field at the CS crossing. Below the primary plot of Figure 1, two smaller plots show details of the storm for two representative 15 minute intervals. The left plot shows an interval before crossing the CS and the right plot after the crossing. The steady outward and inward nature of the radial field can be seen in the B_R component in each of the two smaller plots.

A few isolated Type III bursts are observed prior to the CME eruption at t_0, but there is no sign of continous storm emission. An intense, complex Type III radio burst and a Type II burst start at t_0. The bursts are signatures of electrons accelerated along open field lines (Type III) and by the CME-driven shock (Type II). No significant circular polarization is observed in the intense Type III or in the Type II associated with the CME.

The Type III storm commences near the start of September 6. After approximately 09-06/01:00, Type III emission is

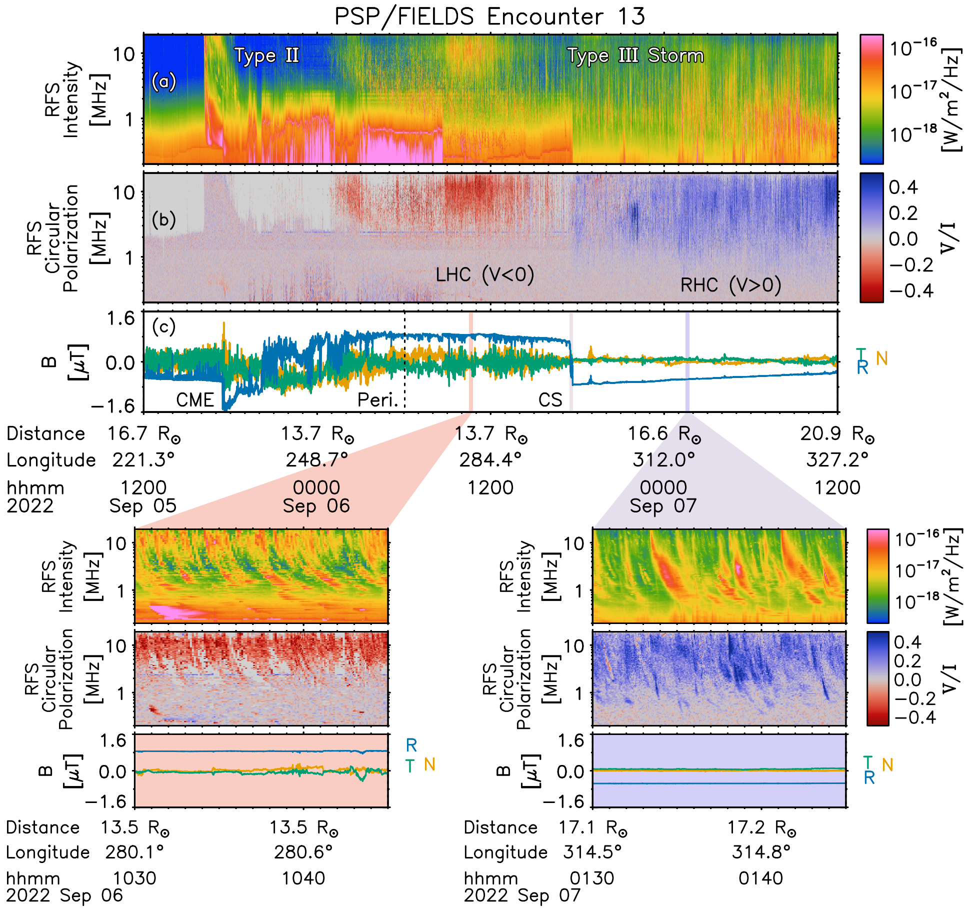

Figure 1. PSP observations of the Type III radio burst storm, which was observed after the CME and Type II radio burst on 2022 September 5. The primary figure shows the intensity (a) and circular polarization (b) of the radio emission, as well as the magnetic field (c). During the storm, the polarization of the emission changes from LHC to RHC, with the shift occurring at the crossing of the heliospheric CS. Secondary figures show short intervals before and after crossing the CS, with LHC (bottom left) and RHC (bottom right) dominated emission.

quasi-continuous, with a consistent LHC polarization. At the time of the CS crossing (boundaries t_{7a} and t_{7b}, indicated in Figure 1(c) with gray shading), the dominant sense of polarization changes from LHC to RHC, corresponding to the change of the magnetic field from outward polarity to inward polarity. The storm continues for the remainder of Encounter 13.

The circular polarization signal is observed at frequencies above ∼1 MHz, while the signal in the intensity spectrogram persists to the plasma frequency (f_p), which ranges from 100 to 300 kHz during the storm interval shown in Figure 1. The concentration of the polarized component at higher frequencies is consistent with previous observations (M. Pulupa et al. 2020), which demonstrate increases in polarization fraction with increasing frequency. The maximum fractional polarization, for both the LHC and RHC intervals, approaches 0.4.

We can compare this observed polarization fraction to previous measurements made at both higher and lower frequencies. Using ground-based observations starting at 24 MHz, G. A. Dulk et al. (1984) observed a bimodal distribution of storm polarization fractions, with the higher peak around a value of 0.4, consistent with the PSP observations at 8–12 MHz. G. A. Dulk et al. (1984) attributed the bimodal distribution to a distinction between storms dominated by fundamental and harmonic emission, with the fundamental associated with the higher fractional polarization. Using Wind data at lower frequencies, M. J. Reiner et al. (2007) reported smaller values of fractional polarization for Type III storms, with typical values below 0.05 at 1 MHz. M. J. Reiner et al. (2007) also demonstrated a strong trend of higher fractional polarization at higher frequency. More recent polarization analysis has primarily focused on isolated Type III bursts. D. E. Morosan et al. (2022) reported polarization levels of 0.4–0.75 for the fundamental component at frequencies of 20–80 MHz. At higher frequencies, M. M. Rahman et al. (2020) reported somewhat lower fractional polarization, with an average value of 0.09 at 80 MHz and 0.22 at 240 MHz. Both reported an increase in fractional polarization with increasing frequency, consistent with the storm observations of M. J. Reiner et al. (2007). Using STEREO observations at frequencies below 2 MHz, V. Krupar et al. (2014) found polarization levels of ≈ 0.1, consistent with instrumental noise levels.

The Wind and STEREO polarization measurements from M. J. Reiner et al. (2007) and V. Krupar et al. (2014) are consistent with the subsequent PSP observations from M. Pulupa et al. (2020), showing negligible polarization levels in individual Type III bursts below several MHz but with storm polarization persisting to lower frequencies. The trend of circular polarization decreasing with decreasing frequency may also be visible in Figure 1. However, we note that this apparent decrease may be affected by increased levels of

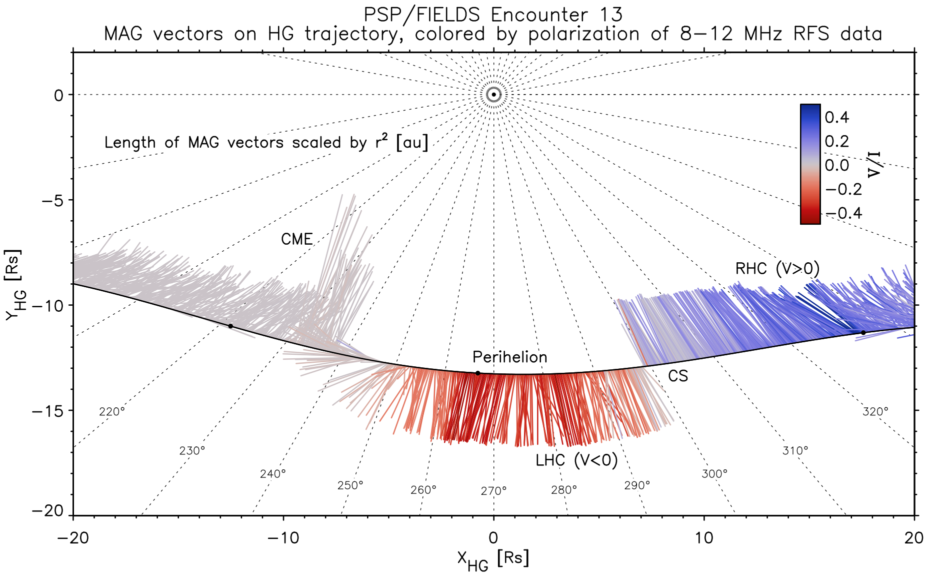

Figure 2. Trajectory of PSP during E13, showing projected magnetic field vectors, with each vector colored according to the circular polarization of radio emission in the 8–12 MHz frequency range. The post-CME field is dominated by the radial component, with LHC emission corresponding to outward polarity of $B_{\rm R}$ and RHC emission corresponding to inward polarity.

in situ quasi-thermal noise (M. Moncuquet et al. 2020; M. M. Martinović et al. 2022) due to the proximity of PSP to the Sun.

Polarization of fundamental plasma emission is driven by the difference between the two electromagnetic modes available for radio emission at frequencies near f_p, the O- and X-modes. The index of refraction for the O-mode allows emission to propagate from the source region to the observer, while X-mode emission is prevented from propagation. The propagating O-mode emission is inherently LHC polarized when traveling along the direction of $\boldsymbol{B}$, consistent with the observations in Figures 1 and 2.

However, IP Type III (and Type II) radio emissions are never observed to be 100% polarized, as this simple picture would imply. Effects of depolarization (D. G. Wentzel 1984; D. B. Melrose 2006) or of generation of emission in both O- and X-modes, simultaneously in inhomogeneous plasma in the presence of density fluctuations (E.-H. Kim et al. 2007), can result in incomplete or near-zero circular polarization.

The distinction between the O- and X-modes is driven by the magnetic field and is most significant when the ratio of cyclotron frequency (ω_e) to plasma frequency ($\omega_p = 2\pi f_p$) is large. Assuming typical scaling in the solar wind, ω_e/ω_p can reach $\sim$0.1 at radial distances corresponding to emission frequencies of $\sim$1 MHz, and it rapidly declines at larger distances/lower frequencies. As the separation between modes becomes less significant, the polarization fraction also decreases. For Type III bursts occurring in regions of low density or enhanced magnetic field (L. Chen et al. 2024), this effect could result in significant polarization persisting to low frequencies.

4. Magnetic Connectivity and Circular Polarization

Figure 2 illustrates the correlation between field direction and measured polarization of radio emission as measured at PSP. The black line plots the trajectory of the spacecraft near perihelion of E13 in Carrington heliographic (HG) coordinates ($X_{\rm HG} - Y_{\rm HG}$). Aside from short time intervals near the CME passage and the CS crossing, the field is nearly radial ($|B| \sim |B_R|$).

The projection of the magnetic field vector into the $X_{\rm HG} - Y_{\rm HG}$ plane is plotted along the spacecraft trajectory. Each vector projection is scaled by r^2 to produce a quantity independent of radial distance, as in S. T. Badman et al. (2021). With the exception of the CME and the CS crossing, the scaled radial field is consistent in magnitude ($B_R\, r^2 \sim$ constant). Each projected vector is also colored according to the circular polarization at 8 MHz. As in Figure 1, this figure shows LHC emission associated with outward field and RHC emission associated with inward field.

The magnetic configuration illustrated in Figure 2 helps to explain the high degree of circular polarization observed in the Type III storm. Previous observations of polarization in RFS data have shown that polarization is an indication of direct connection to the radio source region (T. Nieves-Chinchilla et al. 2022; N. Dresing et al. 2023). Figure 2 is consistent with these observations, with the strongly polarized emission centered around the source region at a Carrington longitude of $\sim$300°.

The storm observations are also consistent with theoretical calculations that show that scattering of radio emission off of regions of enhanced density can destroy circular polarization (D. B. Melrose 2006). D. B. Melrose (2006) demonstrated that this scattering is most effective at destroying circular polarization when the angle between the emission and the density gradient is large. In the solar wind, the density variation that drives scattering is anisotropic and predominantly perpendicular to the magnetic field (E. P. Kontar et al. 2019). Due to this anisotropy, scattered radio emission is preferentially channeled along the magnetic field direction (D. L. Clarkson et al. 2025). With a dominant radial field configuration, as shown in Figure 2, the radio emission generated in a region directly below the observer will be channeled along the radial direction, will experience minimal density variation and minimal scattering, and will therefore suffer minimal depolarization.

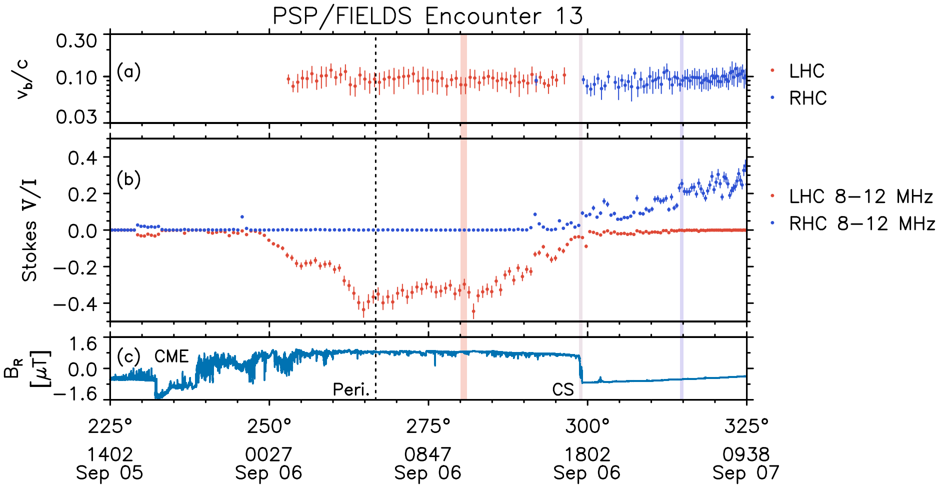

Figure 3. Derived beam speed (a), fractional circular polarization (b), and radial magnetic field (c) as a function of Carrington longitude for the interval shown in Figure 1. The electron beam speed (a) remains consistent throughout the Type III storm interval, for both LHC and RHC intervals. The polarization fraction (b) in both LHC and RHC intervals decreases as the spacecraft approaches the CS. Labels in (c) and vertical interval highlights correspond to the times indicated in Figure 1.

5. Storm Statistics and Longitudinal Dependence

Over the course of the Type III storm, well over 1000 bursts are observed. In both of the 15 minute detail plots from Figure 1, dozens of events are visible. However, it is difficult to clearly separate individual bursts, which often overlap in time and frequency and which also vary widely in amplitude. In this section, we analyze the Type III storm in 15 minute intervals to reveal additional details about the storm-producing active region and the associated accelerated electron beams.

As discussed in the previous section, the most prominent feature of the storm is the abrupt change of emission from LHC to RHC, which indicates the change of source region from the outward polarity magnetic field to inward. We therefore analyze LHC and RHC emissions separately, defining the unnormalized variables V_{LHC} and V_{RHC}:

$$V_{\mathrm{LHC}} = -(V/I) \times I \times H(-V), \tag{1}$$

$$V_{\mathrm{RHC}} = (V/I) \times I \times H(V), \tag{2}$$

where V/I and I are the `STOKES_V` and `PSD_FLUX` variables from the Level 3 RFS data files and H is the Heaviside function. Separating the spectra into V_{LHC} and V_{RHC} allows for independent analysis of each sense of polarization, even when LHC and RHC bursts both occur in a 15 minute interval. Normalized polarization V_{LHC}/I and V_{RHC}/I can also be calculated for each sense. We do note that, in the case of exactly simultaneous emission, the senses of polarization may cancel each other.

Figure 3 shows the beam speed and normalized polarization determined for 15 minute intervals during the CME and subsequent Type III storm. The time interval included in Figure 3 is approximately the same interval as in Figure 1, but Figure 3 uses Carrington longitude as the abscissa rather than time. All LHC-specific quantities are shown in red, while RHC quantities are in blue.

Figure 3(a) shows the beam speed v_{beam}/c, for intervals where an LHC or RHC beam speed could be determined. For each interval, v_{beam} is determined using a time-lag technique developed by N. M. Viall & J. A. Klimchuk (2012) for use in imaging data. In the radio frequency domain, the technique has been applied to modeled radio signatures from closed loops (S. Chhabra et al. 2021) and analysis of Type IIIs observed by PSP (S. Chhabra 2021).

In this study, the time lag between two different frequency channels f_i and f_j from either the V_{LHC} or V_{RHC} data is calculated by identifying the time difference t_{ij}, which maximizes the cross correlation between the frequency channels. The radial distance corresponding to f_i and f_j is calculated by first converting f to electron density, assuming fundamental emission ($f = 9 \times 10^3\sqrt{n_e}$). We assume the emission is fundamental because at these frequencies the fundamental component of Type III bursts tends to be more strongly polarized than the harmonic (I. C. Jebaraj et al. 2023). While S. Chhabra et al. (2021) focused on emission from closed loops, we assume that the post-CME magnetic field lines are open and radial. We can then solve for r from any given f assuming a radial electron density profile. We use the model from Y. Leblanc et al. (1998), which is defined for a nominal electron density of 7.2 cm^{-3} at 1 au:

$$n_e = 3.3 \times 10^5 r^{-2} + 4.1 \times 10^6 r^{-4} + 8.0 \times 10^7 r^{-6}. \tag{3}$$

To determine radial distances based on the PSP E13 measurements, we scale Equation (3) by $(n_{\mathrm{PSP}}/7.2\ \mathrm{cm}^{-3}) \times (r_{\mathrm{PSP}}/215\ R_\odot)^2$, where r_{PSP} is the radial distance of PSP and n_{PSP} is the observed electron density from Level 3 RFS simplified quasi-thermal noise data (M. Moncuquet et al. 2020). The radial distances r_i and r_j corresponding to f_i and f_j can then be determined by solving the scaled version of Equation (3). After determining the time delay and radial distance between two frequency channels, the beam speed is given by

$$v_{ij} = (r_j - r_i)/t_{ij}. \tag{4}$$

The proximity of the spacecraft to the Sun and the radial nature of the magnetic field allow us to ignore any correction for Parker spiral effects in Equation (4).

The polarized emission occurs primarily above 1 MHz, so we calculate beam speeds using the HFR data, which contain 64 frequency channels covering a bandwidth of 1.2–19.2 MHz. After eliminating channel pairs with no significant cross correlation and pairs close in frequency, where the time delay would be shorter than the RFS sampling cadence, valid v_{ij} pairs are averaged to produce a single overall v_{beam} measurement for each 15 minute interval. When the polarized emission in a particular sense is absent or limited during a 15 minute interval, no point is plotted. The beam speeds shown in Figure 3(a) remain steady throughout the storm at $\sim 0.1c$. No significant difference between the LHC (red) and RHC (blue) intervals is apparent.

Initial estimates of Type III storm beam speeds (J. Fainberg & R. G. Stone 1970b) were significantly higher, with an average of $0.38c$. However, beam speed estimates for radio bursts depend on the modeled radial density profile, assumptions regarding the nature of the emission (fundamental versus harmonic), and the beam path length. Since the initial estimates of J. Fainberg & R. G. Stone (1970b), measurements with complementary measurements of electrons and local plasma oscillations have been used to refine these initial estimates and have generally determined lower speeds for radio burst–generating electron beams (R. P. Lin et al. 1981; G. A. Dulk et al. 1987; Y. Leblanc et al. 1998). A speed of $\sim 0.1c$ is consistent with the near-Sun speeds derived by V. Krupar et al. (2015) for individual Type III bursts, using STEREO observations, although we note that M. J. Reiner & R. J. MacDowall (2015) derived somewhat higher speeds using Wind and STEREO measurements.

Figure 3(b) shows time profiles of the circular polarization, over a frequency range from 8 to 12 MHz. As in Figure 3(a), LHC points are plotted in red and RHC in blue, with each point representing a 15 minute interval of data. As discussed in the previous sections, the CS crossing near 300° Carrington longitude separates the LHC and RHC intervals. A gradual decrease in the circular polarization fraction is apparent for both senses of polarization, for longitudes close to the crossing point. The start of the decrease in polarization fraction is most clearly apparent in Figure 3 for the LHC 8–12 MHz data, where a decrease starts at Carrington longitudes between 280° and 285°. The 20° to 25° difference between these longitudes and the CS may be indicative of the width of the emission pattern of the individual storm bursts.

Figure 3(c) shows the radial component of the magnetic field as a reference point for comparison between Figure 3 and the preceding figures. The red, gray, and blue highlighted intervals of Carrington longitude in Figure 3 correspond to the highlighted time intervals in Figure 1.

6. Discussion

From the radio and in situ observations, a picture of the CME and Type III storm emerges. The passage of the CME disturbs the magnetic field in the corona. The post-CME field is highly radial, with a sharp boundary between inward and outward open field lines. On either side of the active region boundary, the configuration of the magnetic field is favorable for quasi-continuous electron acceleration, and the resulting electron beams produce the Type III storm. The Type III emission is directed out along radial field lines, with minimal reflection and scattering. The emission is polarized in the sense consistent with O-mode emission at the fundamental of the local plasma frequency in the source region. The low level of scattering preserves the separation between LHC and RHC intervals and also preserves the polarization signal itself.

Previous coordinated solar flare observations have emphasized the correlation between Type III radio bursts and other flare-related phenomena such as X-ray emission and coronal jets (N. E. Raouafi et al. 2016; A. O. Benz 2017). Individual, nonstorm Type III bursts can be directly associated with EUV jet observations and X-ray emission (e.g., H. M. Bain & L. Fletcher 2009; D. E. Innes et al. 2011; S. Krucker et al. 2011; S. M. Mulay et al. 2016; I. H. Cairns et al. 2018; K.-L. Klein et al. 2022). For smaller-scale flares, each individual energy release is small enough that the overall field configuration is not significantly disturbed and remains capable of electron acceleration and generation of radio emission. Examples of this type of recurrent activity, with Type III bursts accompanied by EUV observations, have been observed by A. R. Paraschiv & A. Donea (2019) and C. Cattell et al. (2021). G. Del Zanna et al. (2011) proposed a model where the continuous burst activity of a Type III storm is driven by active region expansion, which in turn drives interchange reconnection and acceleration of electron beams along these open field lines.

PSP observations of polarized Type III storms, which are are common near the maximum of solar cycle 25, offer an opportunity to test and validate these correlations and models. A majority of encounters since Encounter 8 (2021 April) contain a storm, and all storms show nonzero circular polarization. Future multispacecraft observations using spacecraft equipped with radio, EUV, and X-ray instrumentation (such as Solar Orbiter) offer the opportunity to quantify the energy released during storms and compare to estimates made from larger flares. Multispacecraft radio observations can confirm the angular dependence of the emission pattern suggested in the previous section. Studying many events can establish whether the clear association of the in situ field with the sense of polarization is a universal characteristic of storms, making it a reliable remote diagnostic of the near-Sun magnetic field.

While Type III storms are direct signatures of electron beams, the persistent reconnection that drives the beams and radio emission may also accelerate ions. S. D. Tun Beltran et al. (2015) proposed that Type III storm activity may be a precursor of a CME with high levels of solar energetic particles (SEPs), with the seed particles required for a high-SEP event (J. M. Laming et al. 2013) generated by the same magnetic field configuration that produces the storm. N. Gopalswamy et al. (2022) studied two similar CMEs, one that was preceded by a Type III storm and one that was not. The storm-associated CME indeed showed a significantly higher flux of SEPs, leading to the suggestion that storms are associated with seed particle generation. D. V. Reames (2024) examined the elemental abundance of SEP ions for the event following the storm studied by N. Gopalswamy et al. (2022). However, while they did find evidence of enhanced ^{3}He during the storm interval, they did not find evidence that the storm contributed higher-Z impulsive seed particles to the event.

Future studies incorporating more events are required to fully investigate the possible relationship between Type III storms and SEPs. Although the storm studied in this Letter is not a precursor to an SEP-producing CME, the analysis presented here demonstrates relevant parameters that could contribute to the study of such events. Specifically, a stable Type III beam speed and a sense of polarization consistent with the magnetic field demonstrate evidence for sustained magnetic reconnection and a field configuration that could produce seed particles (S. D. Tun Beltran et al. 2015). Comparing near-Sun energetic particle data to the radio observations could provide direct evidence for a role in storm production of seed particles.

7. Conclusions

Using a Type III radio burst storm observed by PSP, we demonstrate a clear association of the sense of circular polarization with the in situ magnetic field. The sense and degree of circular polarization is consistent with fundamental emission in the *O*-mode. The beam speed, derived from the frequency drift of the Type III storm emission, is steady throughout the duration of the event, consistent with a stable magnetic configuration generating quasi-continuous acceleration of electrons.

The proximity of the spacecraft to the Sun and the quiet radial field observed during this storm allow for a straightforward connection to the inferred source region. The close agreement between the in situ and radio observations indicates that polarized Type III storm observations can be used to remotely probe the magnetic configuration of the source active region. An association between Type III storms and enhanced SEP production has been suggested, but additional observations are required to establish whether such a relationship exists.

Acknowledgments

Parker Solar Probe was designed, built, and is now operated by the Johns Hopkins Applied Physics Laboratory as part of NASA's Living with a Star (LWS) program under NASA contract NNN06AA01C. Data access and processing were done using SPEDAS (V. Angelopoulos et al. 2019). FIELDS data products are publicly available at the FIELDS SOC webpage: https://fields.ssl.berkeley.edu This research was supported by the International Space Science Institute (ISSI) in Bern, through ISSI International Team project No. 557, "Beam-Plasma Interaction in the Solar Wind and the Generation of Type III Radio Bursts." I.C.J. was supported through the Visiting Scientist program of the International Space Science Institute (ISSI) in Bern. The authors thank the anonymous referee for a detailed and constructive review.

ORCID iDs

Marc Pulupa https://orcid.org/0000-0002-1573-7457
Stuart D. Bale https://orcid.org/0000-0002-1989-3596
Immanuel Christopher Jebaraj https://orcid.org/0000-0002-0606-7172
Orlando Romeo https://orcid.org/0000-0002-4559-2199
Säm Krucker https://orcid.org/0000-0002-2002-9180

References

Angelopoulos, V., Cruce, P., Drozdov, A., et al. 2019, SSRv, 215, 9
Badman, S. T., Bale, S. D., Rouillard, A. P., et al. 2021, A&A, 650, A18
Bain, H. M., & Fletcher, L. 2009, A&A, 508, 1443
Bale, S. D., Goetz, K., Harvey, P. R., et al. 2016, SSRv, 204, 49
Benz, A. O. 2017, LRSP, 14, 2
Bougeret, J. L., Fainberg, J., & Stone, R. G. 1984a, A&A, 136, 255
Bougeret, J. L., Fainberg, J., & Stone, R. G. 1984b, A&A, 141, 17
Bougeret, J. L., Goetz, K., Kaiser, M. L., et al. 2008, SSRv, 136, 487
Bougeret, J. L., Kaiser, M. L., Kellogg, P. J., et al. 1995, SSRv, 71, 231
Cairns, I. H., Lobzin, V. V., Donea, A., et al. 2018, NatSR, 8, 1676
Cattell, C., Glesener, L., Leiran, B., et al. 2021, A&A, 650, A6
Cecconi, B., Bonnin, X., Hoang, S., et al. 2008, SSRv, 136, 549
Chen, L., Ma, B., Wu, D., et al. 2024, ApJ, 961, 136
Chhabra, S. 2021, PhD Thesis, New Jersey Institute of Technology
Chhabra, S., Klimchuk, J. A., & Gary, D. E. 2021, ApJ, 922, 128
Clarkson, D. L., Kontar, E. P., Chrysaphi, N., et al. 2025, NatSR, 15, 11335
Del Zanna, G., Aulanier, G., Klein, K. L., & Török, T. 2011, A&A, 526, A137
Dresing, N., Rodríguez-García, L., Jebaraj, I. C., et al. 2023, A&A, 674, A105
Dulk, G. A. 2000, GMS, 119, 115
Dulk, G. A., Goldman, M. V., Steinberg, J. L., & Hoang, S. 1987, A&A, 173, 366
Dulk, G. A., Suzuki, S., & Sheridan, K. V. 1984, A&A, 130, 39
Eastwood, J. P., Wheatland, M. S., Hudson, H. S., et al. 2010, ApJL, 708, L95
Fainberg, J., & Stone, R. G. 1970a, SoPh, 15, 222
Fainberg, J., & Stone, R. G. 1970b, SoPh, 15, 433
Fainberg, J., & Stone, R. G. 1971, SoPh, 17, 392
Fox, N. J., Velli, M. C., Bale, S. D., et al. 2016, SSRv, 204, 7
Gopalswamy, N. 2004, P&SS, 52, 1399
Gopalswamy, N., Akiyama, S., Mäkelä, P., Yashiro, S., & Xie, H. 2022, in 3rd URSI Atlantic and Asia Pacific Radio Science Meeting (AT-AP-RASC) (Piscataway, NJ: IEEE)
Gurnett, D. A., Kurth, W. S., Kirchner, D. L., et al. 2004, SSRv, 114, 395
Hamaker, J. P., & Bregman, J. D. 1996, A&AS, 117, 161
Harra, L., Brooks, D. H., Bale, S. D., et al. 2021, A&A, 650, A7
Innes, D. E., Cameron, R. H., & Solanki, S. K. 2011, A&A, 531, L13
Jebaraj, I. C., Krasnoselskikh, V., Pulupa, M., Magdalenic, J., & Bale, S. D. 2023, ApJL, 955, L20
Kim, E.-H., Cairns, I. H., & Robinson, P. A. 2007, PhRvL, 99, 015003
Klein, K.-L., Musset, S., Vilmer, N., et al. 2022, A&A, 663, A173
Kontar, E. P., Chen, X., Chrysaphi, N., et al. 2019, ApJ, 884, 122
Krucker, S., Kontar, E. P., Christe, S., Glesener, L., & Lin, R. P. 2011, ApJ, 742, 82
Krupar, V., Kontar, E. P., Soucek, J., et al. 2015, A&A, 580, A137
Krupar, V., Maksimovic, M., Santolik, O., Cecconi, B., & Kruparova, O. 2014, SoPh, 289, 4633
Laming, J. M., Moses, J. D., Ko, Y.-K., et al. 2013, ApJ, 770, 73
Leblanc, Y., Dulk, G. A., & Bougeret, J.-L. 1998, SoPh, 183, 165
Lecacheux, A. 2011, in Proc. of the 7th Int. Workshop on Planetary, Solar and Heliospheric Radio Emissions, ed. H. O. Rucker et al. (Vienna: Austrian Academy of Sciences), 13
Lin, R. P. 1985, SoPh, 100, 537
Lin, R. P., Potter, D. W., Gurnett, D. A., & Scarf, F. L. 1981, ApJ, 251, 364
Ma, B., Chen, L., Wu, D., et al. 2025, ApJ, 979, 22
Martinović, M. M., Dordević, A. R., Klein, K. G., et al. 2022, JGRA, 127, e2021JA030182
Melrose, D. B. 2006, ApJ, 637, 1113
Moncuquet, M., Meyer-Vernet, N., Issautier, K., et al. 2020, ApJS, 246, 44
Morioka, A., Miyoshi, Y., Masuda, S., et al. 2007, ApJ, 657, 567
Morosan, D. E., Räsänen, J. E., Kumari, A., et al. 2022, SoPh, 297, 47
Mulay, S. M., Tripathi, D., Del Zanna, G., & Mason, H. 2016, A&A, 589, A79
Nieves-Chinchilla, T., Alzate, N., Cremades, H., et al. 2022, ApJ, 930, 88
Page, B., Bassett, N., Lecacheux, A., et al. 2022, A&A, 668, A127
Paraschiv, A. R., & Donea, A. 2019, ApJ, 873, 110
Pulupa, M., Bale, S. D., Badman, S. T., et al. 2020, ApJS, 246, 49
Pulupa, M., Bale, S. D., Bonnell, J. W., et al. 2017, JGRA, 122, 2836
Rahman, M. M., Cairns, I. H., & McCauley, P. I. 2020, SoPh, 295, 51
Raouafi, N. E., Patsourakos, S., Pariat, E., et al. 2016, SSRv, 201, 1
Reames, D. V. 2024, FrASS, 11, 1368043
Reid, H. A. S., & Ratcliffe, H. 2014, RAA, 14, 773
Reiner, M. J., Fainberg, J., Kaiser, M. L., & Bougeret, J. L. 2007, SoPh, 241, 351
Reiner, M. J., Kaiser, M. L., Karlický, M., Jiřička, K., & Bougeret, J. L. 2001, SoPh, 204, 121
Reiner, M. J., & MacDowall, R. J. 2015, SoPh, 290, 2975
Robishaw, T., & Heiles, C. 2021, in The WSPC Handbook of Astronomical Instrumentation, Volume 1: Radio Astronomical Instrumentation, ed. A. Wolszczan (Singapore: World Scientific), 127
Romeo, O. M., Braga, C. R., Badman, S. T., et al. 2023, ApJ, 954, 168
Sishtla, C. P., Jebaraj, I. C., Pomoell, J., et al. 2023, ApJL, 959, L33
Tun Beltran, S. D., Cutchin, S., & White, S. 2015, SoPh, 290, 2423
Viall, N. M., & Klimchuk, J. A. 2012, ApJ, 753, 35
Wentzel, D. G. 1984, SoPh, 90, 139